Supporting information

Dimensional Engineering to Simultaneously Enhance Energy Density and Stability of MAPbBr3 based Photo-rechargeable Ion Capacitor

Tanuj Kumar[a], Rahul Thakuria[a], Mohit Kumar[a], Ankush Kumar[a,b], Ramesh Kumar[a,c,*] and Monojit Bag[a,d,*]

a Advanced Research in Electrochemical Impedance Spectroscopy Laboratory, Indian Institute of Technology Roorkee, Roorkee 247667, India

b School of Physics and Mathematical Sciences, Nanyang Technological University Singapore, 21 Nanyang link, Singapore 637371

c Department of Chemistry, Ångström Laboratory, Uppsala University, Box 523, SE, 75120 Uppsala, Sweden

d Centre for Nanotechnology, Indian Institute of Technology Roorkee, Roorkee 247667, India

Corresponding author: *(Monojit Bag) monojit.bag@ph.iitr.ac.in

*(Ramesh Kumar) rkumar1@ph.iitr.ac.in

1. Materials and method

Materials

Lead (II) Bromide $PbBr_2$ (>98%, Sigma Aldrich), methyl ammonium bromide (CH_3NH_3Br 99.6%, TCI Chemicals), Phenethyl ammonium bromide (>98%, Sigma Aldrich), chlorobenzene (anhydrous 99.8%), Dimethylformamide (DMF, anhydrous ≥99.8%, Sigma-Aldrich), Poly-vinylidene fluoride (PVDF, Sigma-Aldrich), Super P (carbon black,acetylene, 100% compressed, 99.9%,Alfa Aeser), and N-methyl-pyrrolidone (NMP, 99.9%, Sigma-Aldrich), Dichloromethane (DCM), Tetrabutylammonium tetrafluoroborate (TBATFA) were used.

Electrolyte Preparation

To prepare the liquid electrolyte, we took 10 ml Dichloromethane (DCM) (anhydrous, ≥99.8%, Sigma Aldrich) and transferred it into a vial. 329 mg of Tetrabutylammonium tetrafluoroborate (TBATFA) was measured using a digital balance and added to the DCM. This mixture of DCM and TBATFA was stirred.

Electrode Preparation and Electrochemical Characterization.

Using the vacuum oven, we synthesized 3D ($CH3NH_3PbBr_3$) and 2D (PEA_2PbBr_4) single crystals in a DMF solution. $CH_3NH_3PbBr_3$ single crystal was synthesized using inverse temperature crystallization and (PEA_2PbBr_4) single crystal growth was done using the slow cooling method in which temperature was decreased from 60 ^0C to room temperature. Then the solution was left at room temperature for a few days (4 days). Firstly, we ground the single crystal of 3D and 2D separately for 40 minutes to make a homogeneous powder. Then we mixed the 2D powder into 3D powder in different ratios. Four types of electrodes were made by mixing these different dimensional single crystal powders. These electrodes are named as **D0** (Pure 3D), **D5** (5% weight mass of 2D in 3D), **D10** (10% weight mass of 2D in

3D), **D20** (20% weight mass of 2D in 3D). Before preparing the electrode, we mixed these synthesized single powders (75%) with activated carbon (Black carbon 10%) and Polyvinylidene fluoride (PVDF) (15%). The PVDF was used as a binder. This mixer was transferred in a vial of 5ml containing NMP (N-Methyl-2-pyrrolidone) and was stirred magnetically for 10 to 12h to prepare the smooth and homogeneous slurry for the active electrode. On a conducting graphite sheet, this slurry was uniformly coated by using a brush and this coated electrode was annealed to vaporize the NMP solvent at ~80 ^{0}C for 3 h.

Material characterization

Carl Zeiss Ultra Plus Field-Emission Scanning Electron Microscopy (FESEM) was used to measure the size of the crystallites of the powder of single crystals and to study the morphology of the surface of the fabricated electrodes. The structural analysis was performed using an X-ray diffractometer (XRD D8 Advance) with Cu K_α radiation of wavelength 1.54 Å and the angle between the diffracted rays and incident rays were varied from 5−60°C in steps of 0.02^0. The crystallite size and micro-strain were determined from the XRD spectra of these powders.

Electrochemical characterization

All the electrochemical cell characterization such as cyclic voltammetry (CV) and Galvanostatic Charge-Discharging (GCD) measurement of the devices was carried out on Metrohm Autolab PGSTAT204 (100-200V) which was equipped with NOVA 2.1 software by a typical three-electrode system : a reference electrode, counter electrode and a working electrode (perovskite active electrode) where redox reactions take place. Using the same equipment, electrochemical impedance spectroscopy (EIS) was carried out at zero bias vs Ag/AgCl on both perovskite electrodes to better understand the electronic-ionic dynamics. By using curve plotted by the data of CV, one can distinguish between the two types of capacitive

behaviour (Faradic and Non-faradic) of the electrode. Ag/AgCl was used as a reference electrode in 3M KCl and platinum was used as the counter electrode.

2. Calculations

2.1 The Specific capacitance (F g^{-1}) were calculated from the CV and GCD spectra using the following relations

$$C_S(F / g) = \frac{\int i \, dV}{\Delta V \times v \times m} \qquad \text{(From the CV spectra)} \qquad \text{S1}$$

$$C_S = \frac{I \Delta t}{m \Delta V} \qquad \text{(From the GCD spectra)} \qquad \text{S2}$$

2.2 The energy density and power density of photo-electrochemical cells were calculated in the dark and under light according to following equations

$$E = \frac{1}{7.2} \times C_s (\Delta V)^2 \qquad \text{S3}$$

$$P = \frac{E}{t} \qquad \text{S4}$$

Where, C$_s$ is the specific capacitance in the dark/light, $\int i \, dV$ is the active area under CV spectra, ΔV is potential window (V), υ is the scan rate (mV s^{-1}) and t is the galvanostatic discharging time and m is mass of the active material (g).

For the quantification of EDLC and diffusion limited processes, we have decoupled equation 2 into two parts according to following relation

$$i_p = k_1 v + k_2 v^{\frac{1}{2}} \qquad \text{S5}$$

For the analytical purposes, we can rearrange equation S5

$$\frac{i_p}{v^{\frac{1}{2}}} = k_1 v^{\frac{1}{2}} + k_2$$

B-M Approximation-

Using the Nyquist plots one can find the value of the loss tangent using the following equation.

$$tan(\Phi) = \frac{Z'}{Z''} \tag{6}$$

The value of the ion-diffusion coefficient is found by using the equation given by B-M approach:

$$D_{ion} = \frac{L^2}{\tau\delta^2} \tag{7}$$

Where, D is the diffusion ion coefficient and L is the thickness of the electrode on the conducting graphite sheet. ..

The value of L was measured by the cross section FESEM image of the active electrode as shown in **Figure 2(f)** was found to be ~5 μm.

The value of δ is found by using the plot between tan (Φ) vs frequency by using the following equation:

$$tan(\phi)_m = \frac{\sqrt{\delta}}{2} \tag{8}$$

The Debye length was calculated using the following formulae:

$$\lambda = (D_{ion}\tau_2)^{1/2} \tag{9}$$

Where, λ is the Debye-length, τ_2 is the time-constant which was calculated to the frequency corresponding to the peak in the loss tangent curve between tan (Φ) vs frequency.

Under dark, the variation in the calculated value of the ion-diffusion coefficient for all devices has been shown in the **Figure S (15)**.

Capacitance-frequency (C-F) analysis-

As a function of frequency (f), we can determine the real and imaginary values of capacitance (C' and C'') using the values of the real and imaginary (Z' and Z'') impedances. For this we can use the following equations:

$$C' = -\frac{Z''}{2\pi f |Z|^2} \tag{10}$$

$$C'' = \frac{Z'}{2\pi f |Z|^2} \tag{11}$$

Z is the resultant value of complex impedance in Ωs.

$$Z = \sqrt{(Z')^2 + (Z'')^2} \tag{12}$$

We measured the CV of all electrodes in dark and illuminated conditions at different scanning rates ranging from 5 to 160 mV s^{-1}.
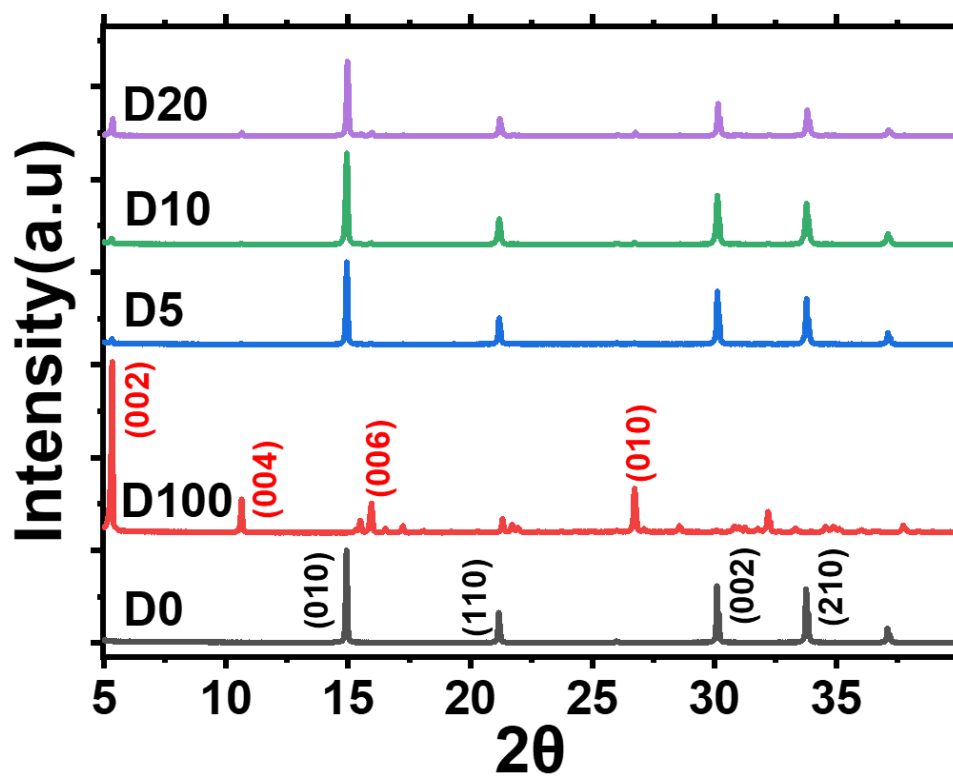
Figure S1: The XRD pattern of perovskite powder with different mass % of 2D-perovskite in 3D perovskite.
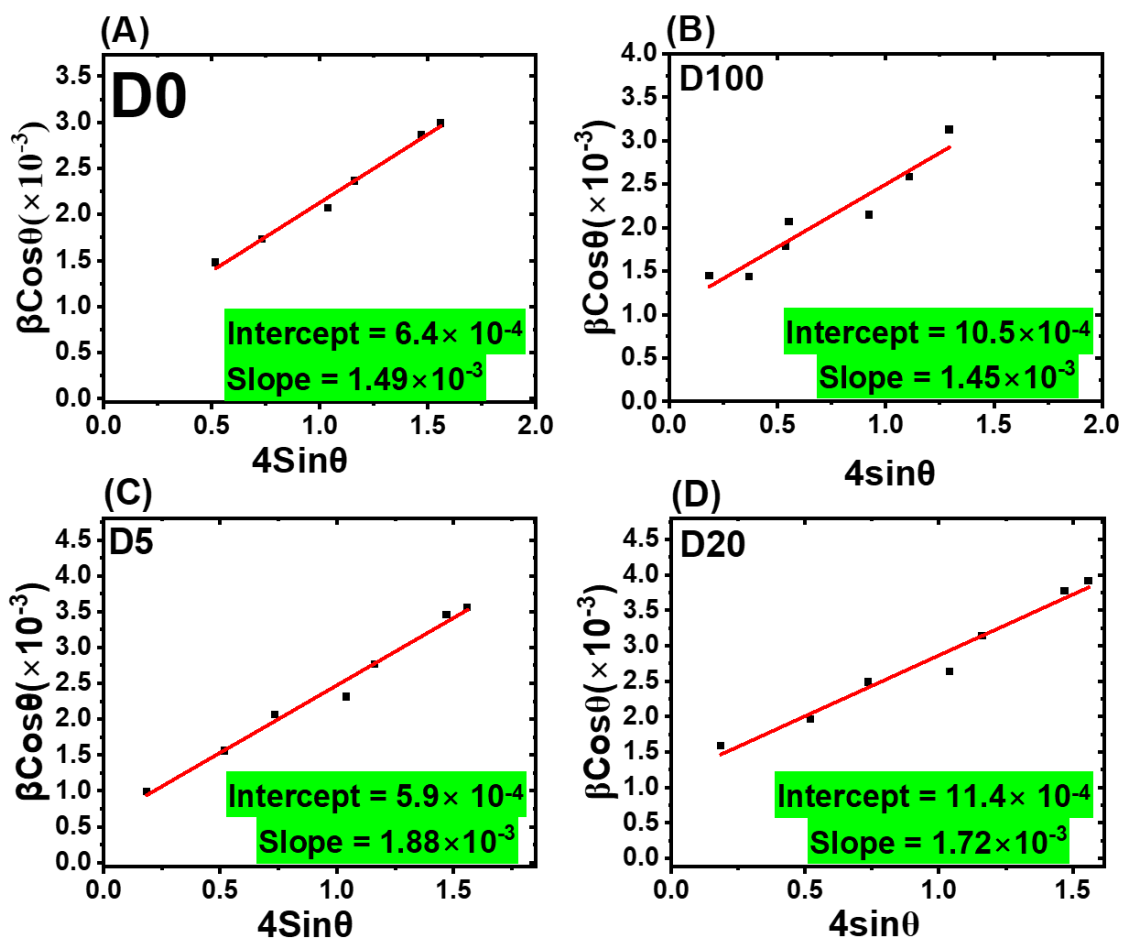
Figure S2: W-H plots of the as prepared powder of (A) pure $MAPbBr_3$ (B) pure $(PEA)_2PbBr_4$ powder (C) D5 (5% 2D perovskite) (D) D20 (20% 2D perovskite)
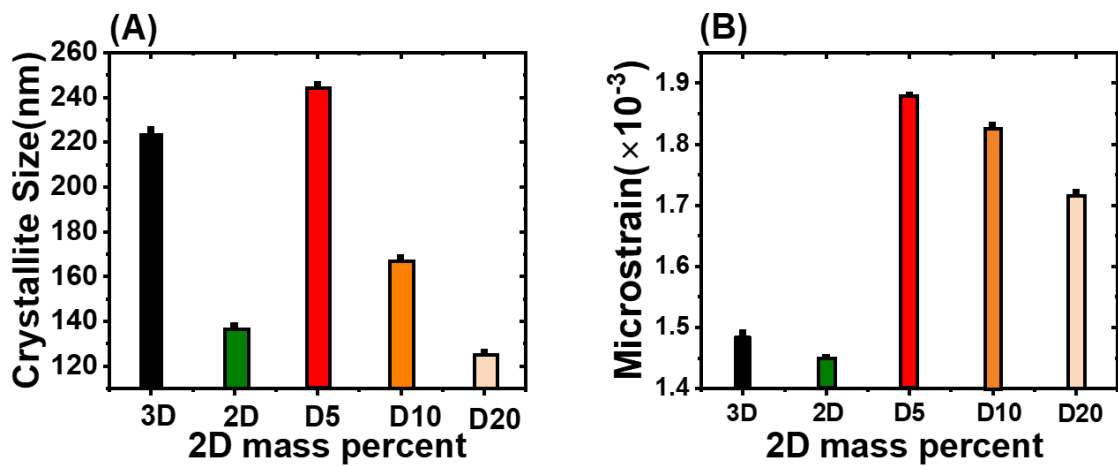
Figure S3: Comparison between the (A) Crystallite size and (B) Micro-strain calculated by the W-H plots for the powder of all samples.
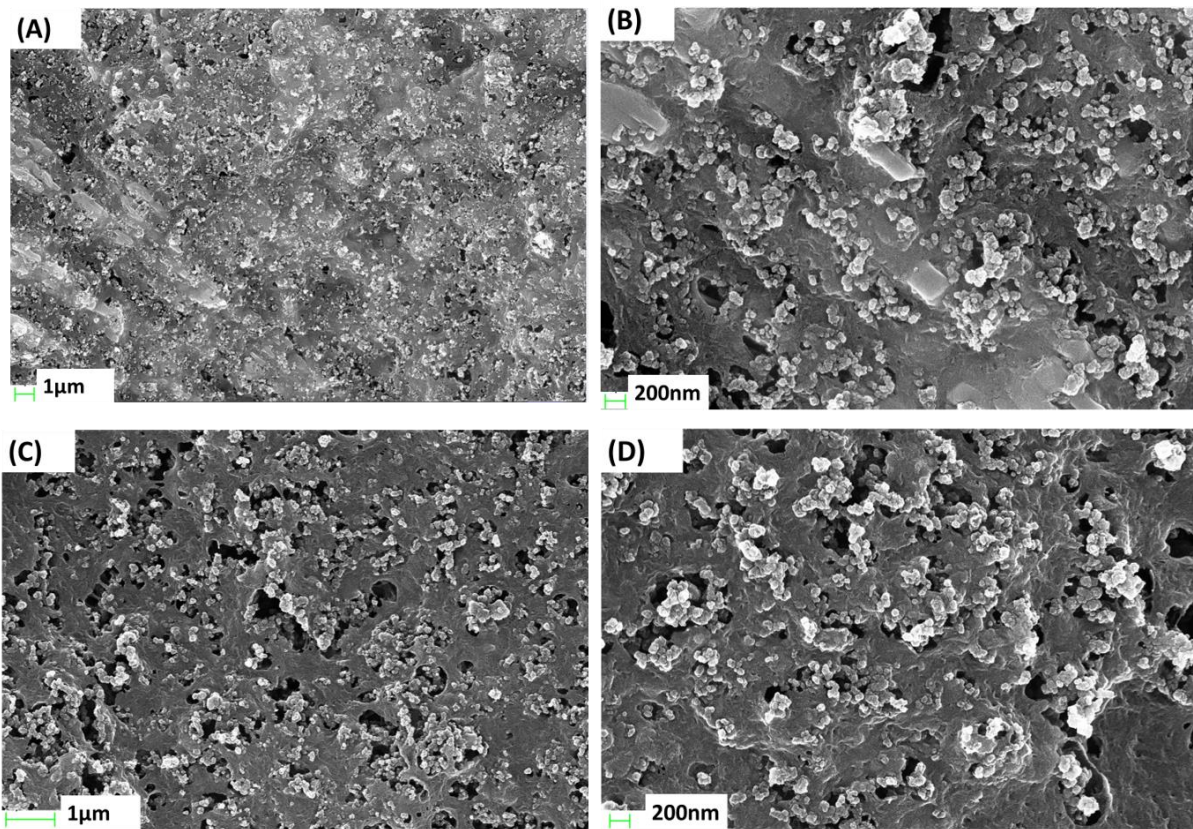
Figure S4: Top view FE-SEM images of the electrodes of (A & B) pure MAPbBr$_3$ (D0) electrodes and (C & D) pure (PEA)$_2$PbBr$_4$ (D100) electrodes showing no flakes formation.
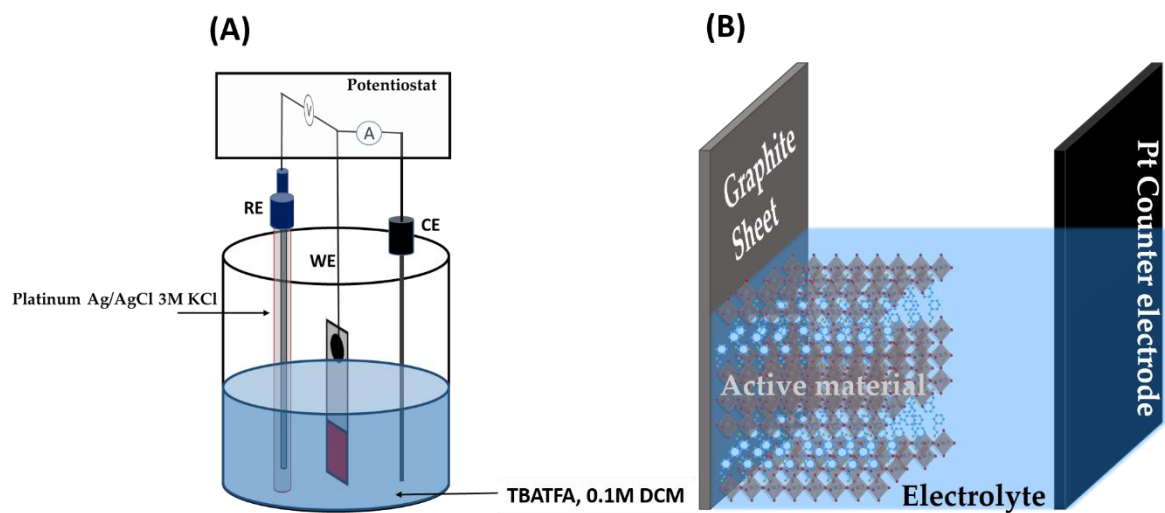
Figure S5: Schematic Diagram of the setup of electrochemical measurements.
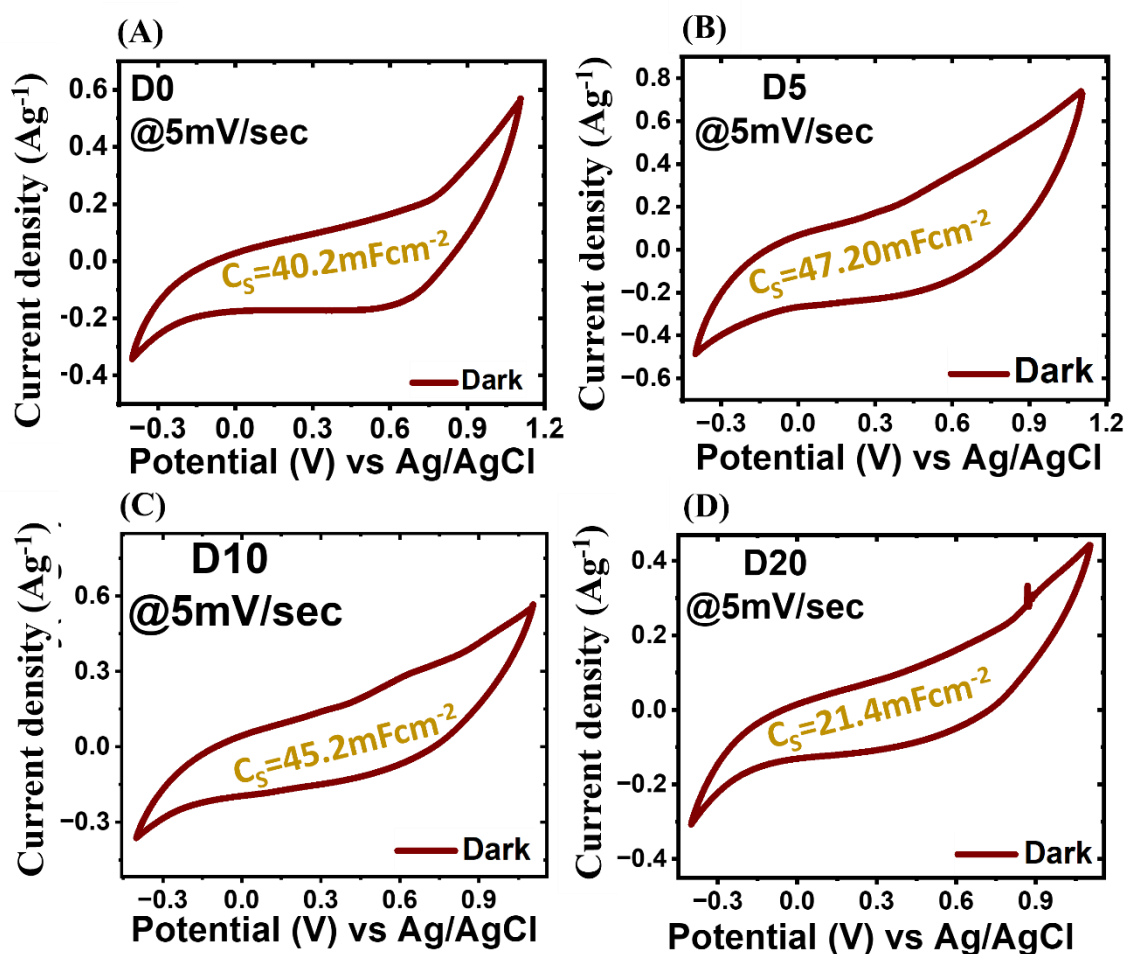
Figure S6: CV responses in dark conditions for all D-samples. CV curve at scan rate of 5mV/s for (A) Pure bulky 3D device (D0) (B) 5% mass of 2D in 3D (D5) (C) 10% mass of 2D in 3D (D10) and (D) 20% mass of 2D in 3D (D20). Scan rate = 5 mVs^{-1}. The value of the specific capacitance (Cp) calculated by the GCD curves are shown for all samples.
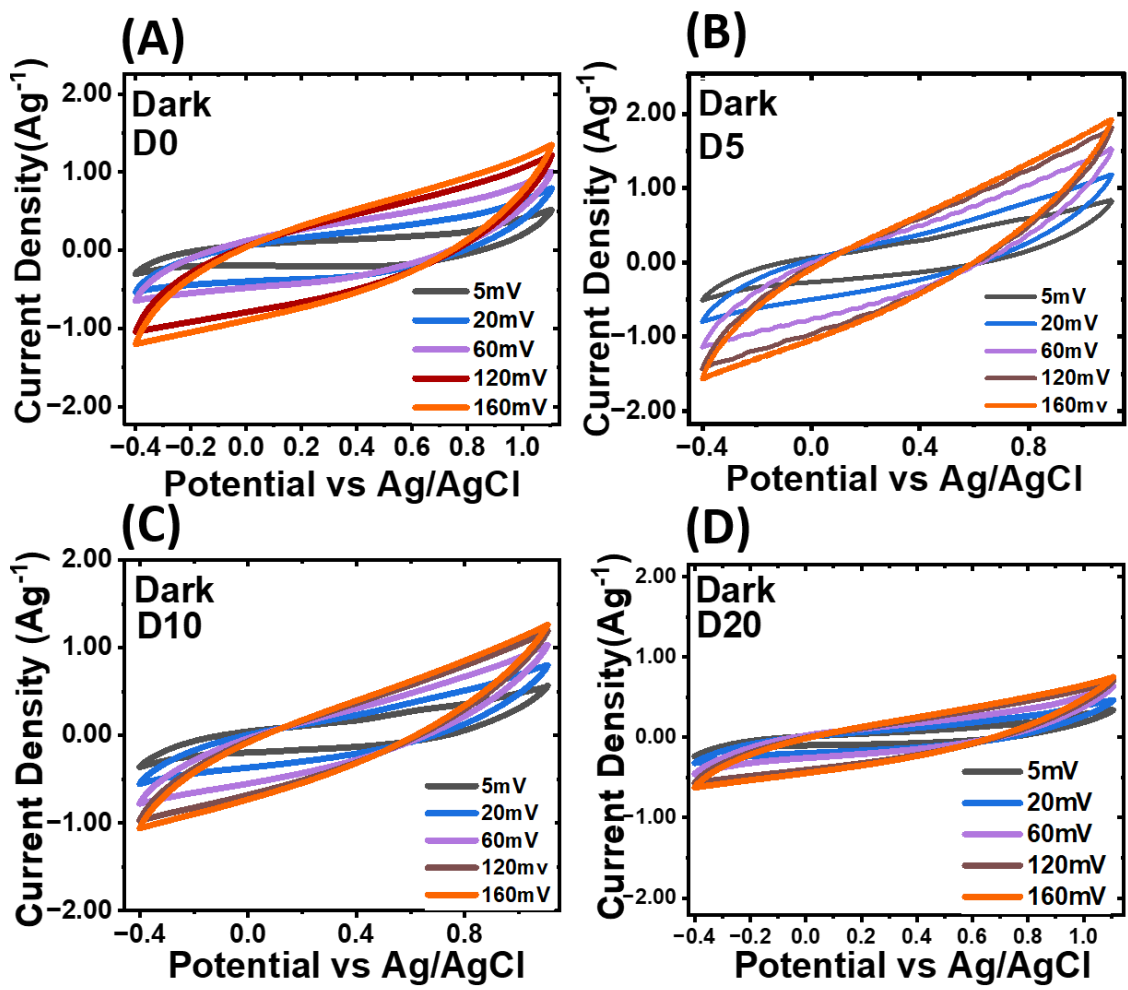
Figure S7: CV responses in dark conditions for all D-samples. CV curve at scan rate at different scan rates varying from 5mV/s to 160mV/s for (A) Pure bulky 3D device (D0) (B) 5% mass of 2D in 3D (D5) (C) 10% mass of 2D in 3D (D10) and (D) 20% mass of 2D in 3D (D20).
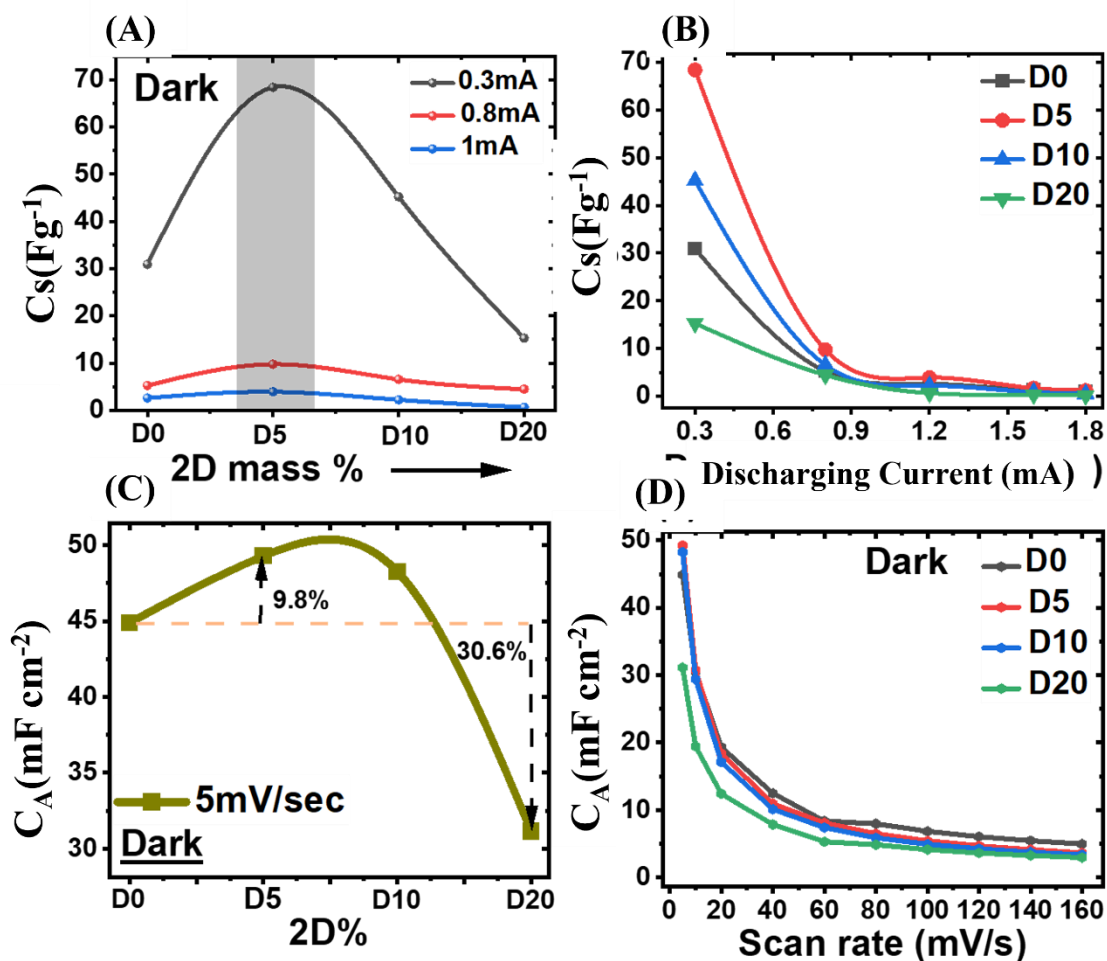
Figure S8. Electrochemical cell performance for all electrodes, (A) The variation of specific capacitance (C_s) all D-samples under dark condition with the discharging current 0.3 mA, 0.8 mA and 1 mA. (b)The variation in the calculated values of the (B) specific capacitance with the different discharging current (C) The areal capacitance (C_A) for the all D-samples at 5mVs^{-1} in dark using CV curve. (D) The areal capacitance for all the D-samples at different voltage scan rates under dark conditions.

Table S1: The various parameter of the all D- samples in the dark-condition.

Parameters	D0	D5	D10	D20
Areal Capacitance	40.2 mFcm^{-2}	**47.2 mFcm^{-2}**	45.2 mFcm^{-2}	21.4 mFcm^{-2}
Specific Capacitance	30.92 Fg^{-1}	**68.4 Fg^{-1}**	45.2 Fg^{-1}	15.2 Fg^{-1}
Specific Energy Density	9.6 Whkg^{-1}	**21.37 Whkg^{-1}**	14.12 Whkg^{-1}	4.7 Whkg^{-1}
Specific Power Density @ 0.8 mA cm-2	461.5 Wkg^{-1}	**869.5 Wkg^{-1}**	600 Wkg^{-1}	407 Wkg^{-1}
Cyclic Stability	-	**90%**	94%	97%

Table S2: The various parameter of the all D- samples under illumination.

Parameters	D0	D5	D10	D20
Areal Capacitance	45.6 mFcm^{-2}	50.0 mFcm^{-2}	**75.8 mFcm^{-2}**	18 mFcm^{-2}
Specific Capacitance	35.07 Fg^{-1}	72.4 Fg^{-1}	**75.8 Fg^{-1}**	12.85 Fg^{-1}
Specific Energy Density	10.96 Whkg^{-1}	22.64 Whkg^{-1}	**23.68 Whkg^{-1}**	4.01 Whkg^{-1}
Specific Power Density @ 0.8 mA cm-2	461.5 Wkg^{-1}	869.5 Wkg^{-1}	**600 Wkg^{-1}**	407 Wkg^{-1}
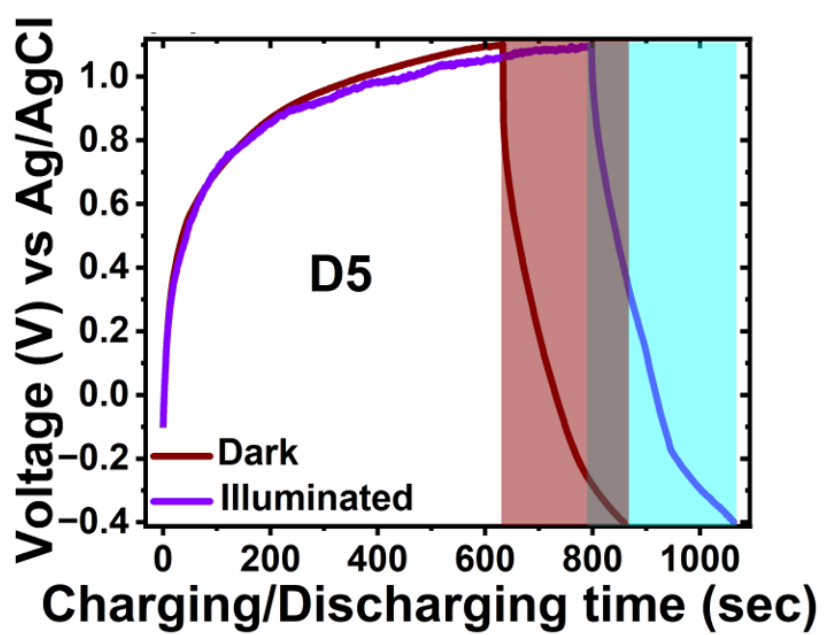
Figure S9. GCD curve for the D5 sample under dark and illuminated conditions
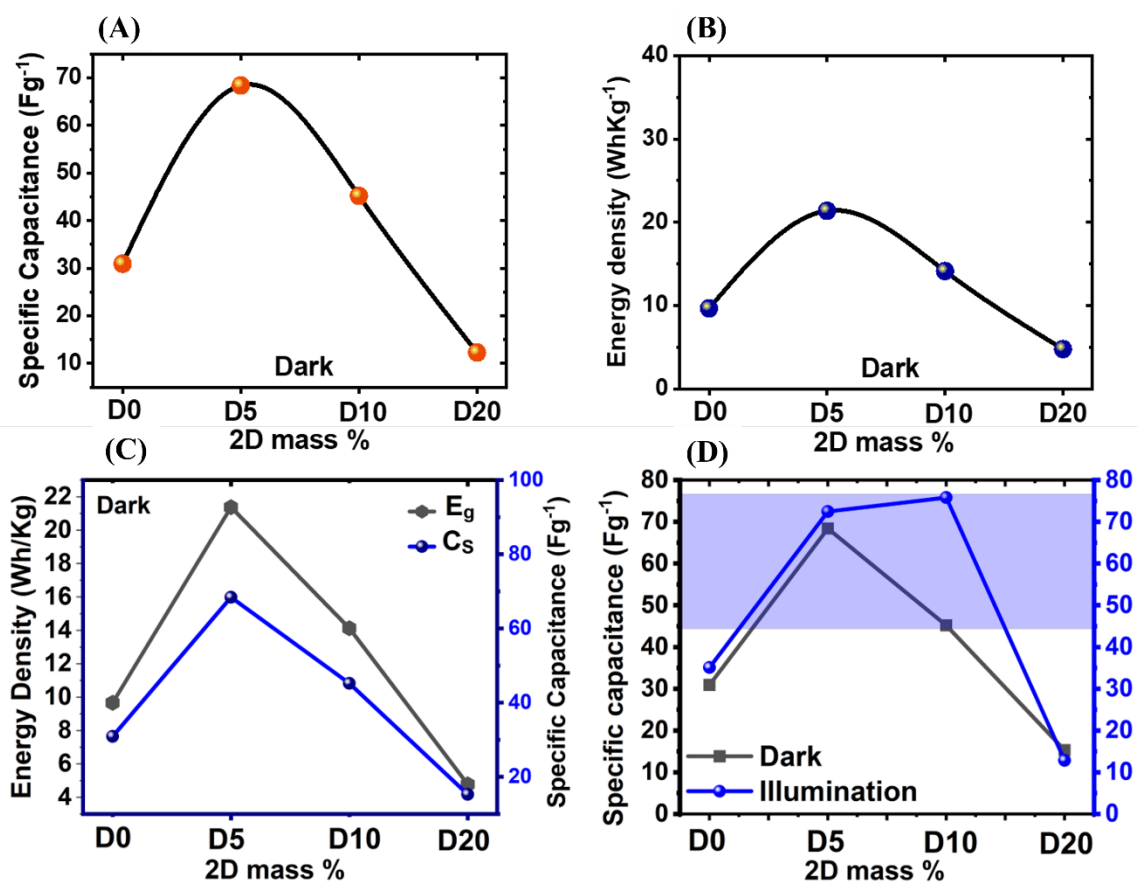
Figure S10. (A) Specific capacitance and (B) energy density measured by GCD curves under dark-conditions for all D-samples (C) Energy density and specific capacitance and (D) The specific capacitance under dark and illuminated condition.
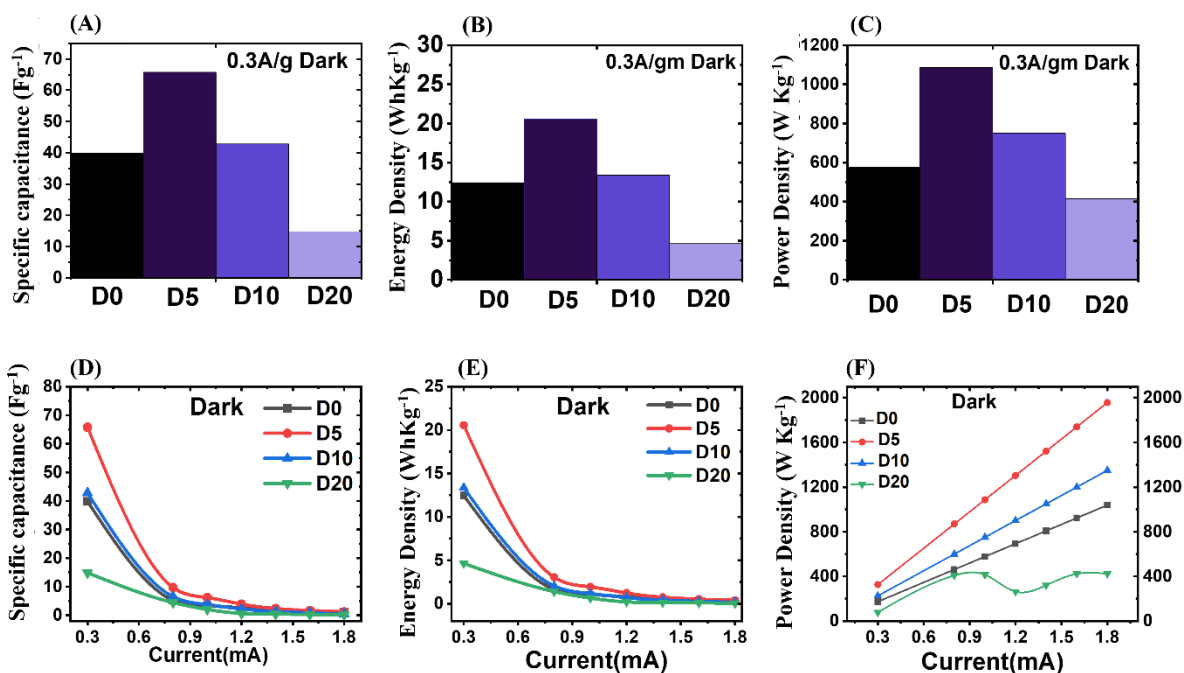
Figure S11. The comparison between the all samples and their values of (A) specific capacitance @0.3mA (B) energy density @0.3mA and (C) power at the discharging current @0.8mA . The variation in the (D) specific capacitance, (E) energy density @0.3mA and (F) power density @0.8mA with the different discharging current.
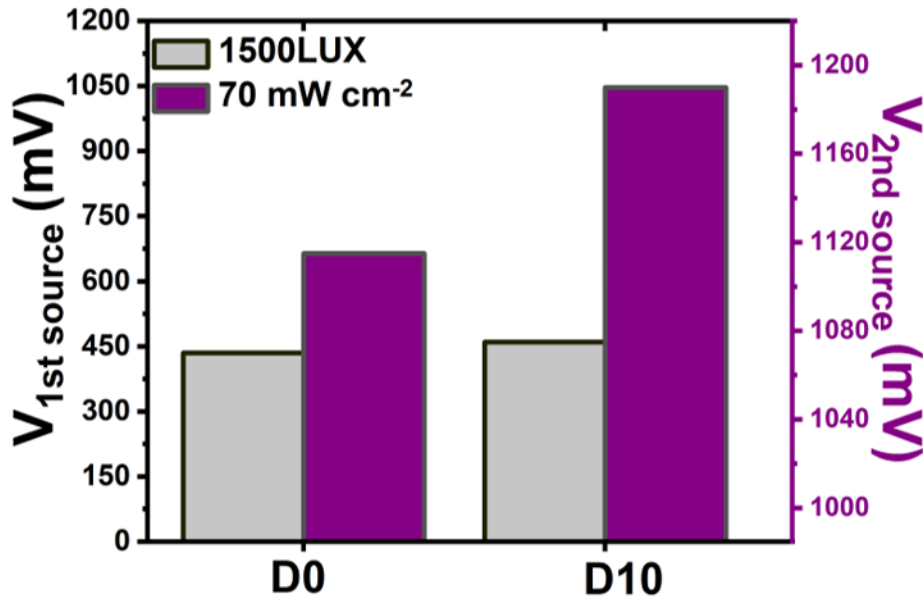
Figure S12. The comparison of the photo-potential under the two different sources (1st source = 1500 Lux and 2nd source = 70 mW cm^{-2} of 405nm) between the photo-chargeable ion capacitor based on pure 3D perovskite material (D0) and 2D/3D heterostructure based electrode.
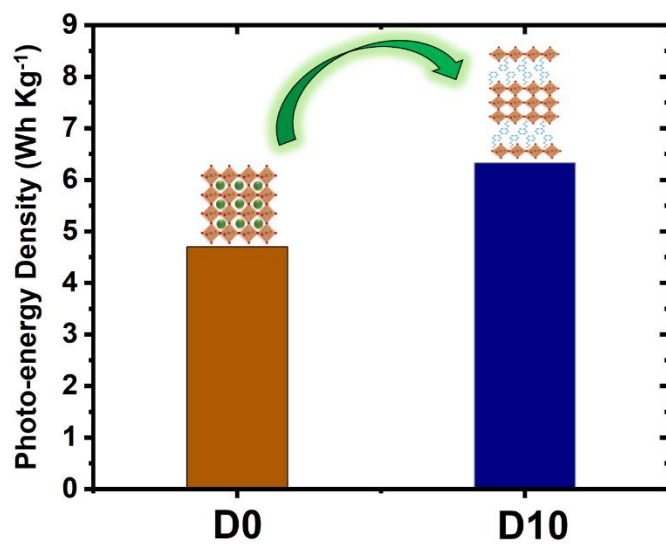
Figure S13. The comparison of the photo-energy density under 2nd source (70 mW cm^{-2} of 405nm) between the photo-chargeable ion capacitor based on pure 3D perovskite material (D0) and 2D/3D heterostructure based electrode.
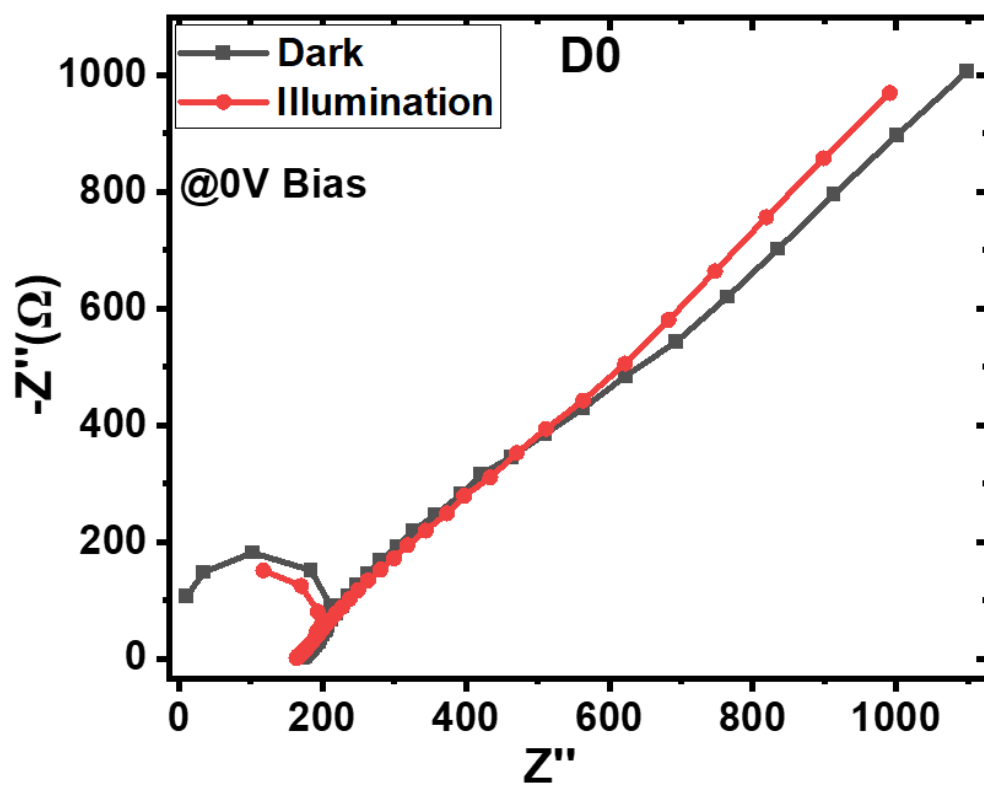
Figure S14. Electrochemical impedance spectroscopy (EIS) Nyquist plots under dark (black) and illuminated (red) conditions at bias of 0 volt for device D0.
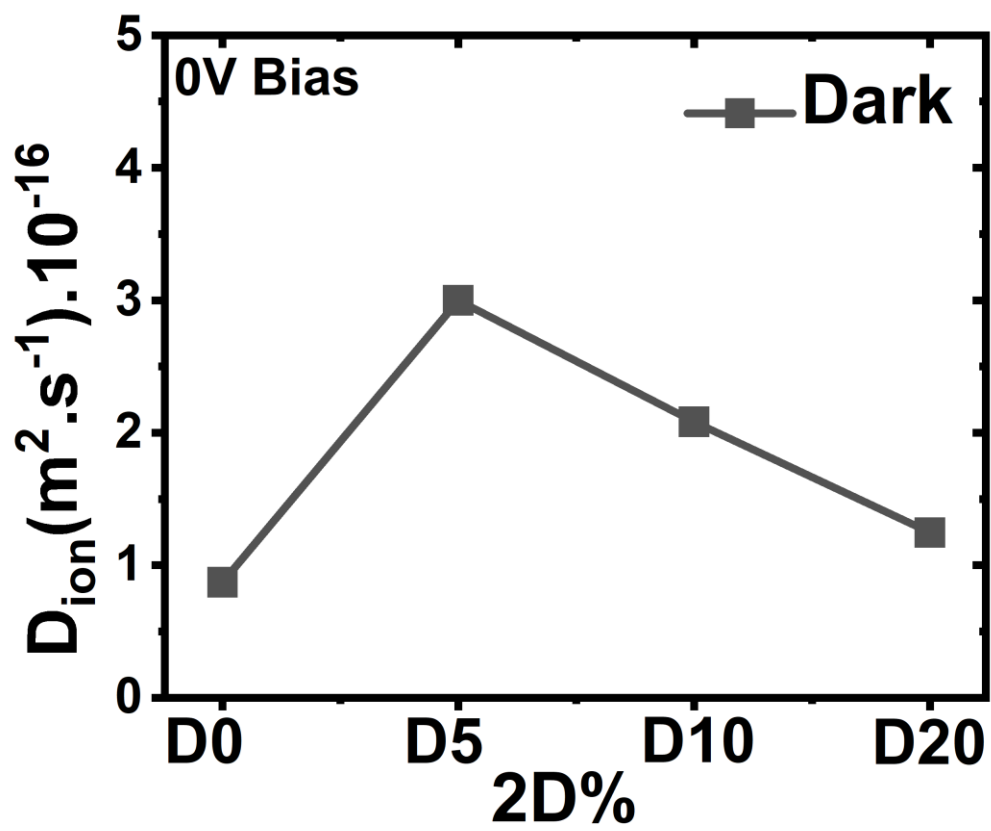
Figure S15. Ion-diffusion coefficient under dark for the all D-samples
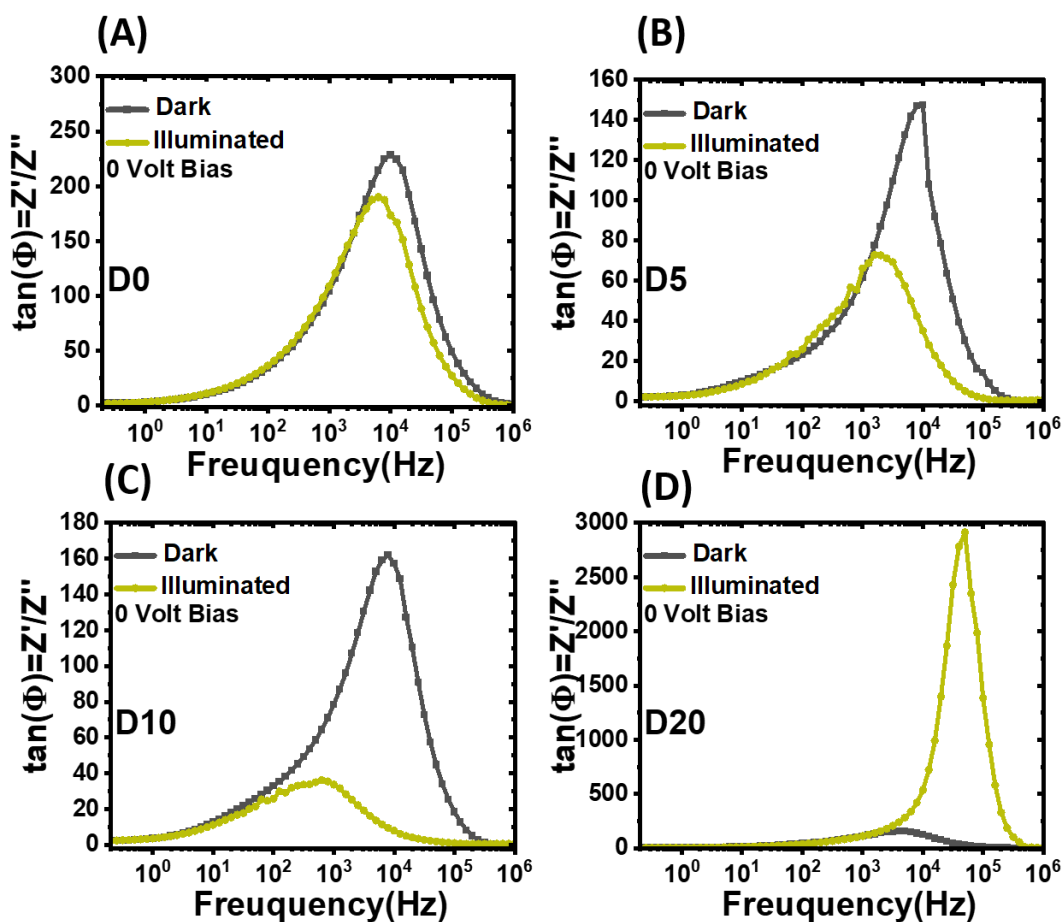
Figure S16. Comparison of the curve between the value of tan(Φ) with respect to the frequency under dark and illuminated condition for the sample (A) D0, (B) D5, (C) D10 and (D) D20. The value was calculated using the EIS curved which was performed at 0 V bias under dark and illumination.
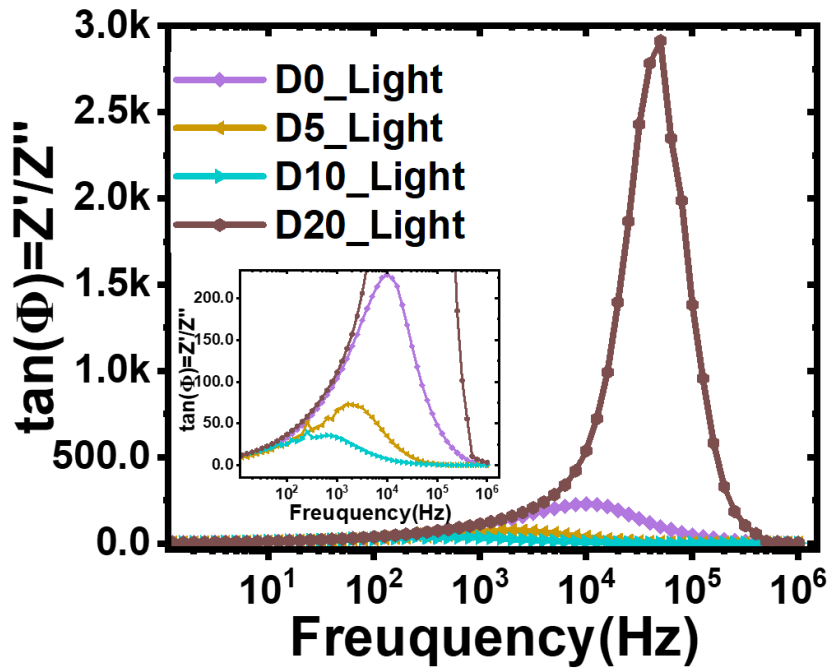
Figure S17. The curve between tan (Φ) and frequency from 0.01Hz to 10^6 Hz for all D-samples under illumination.
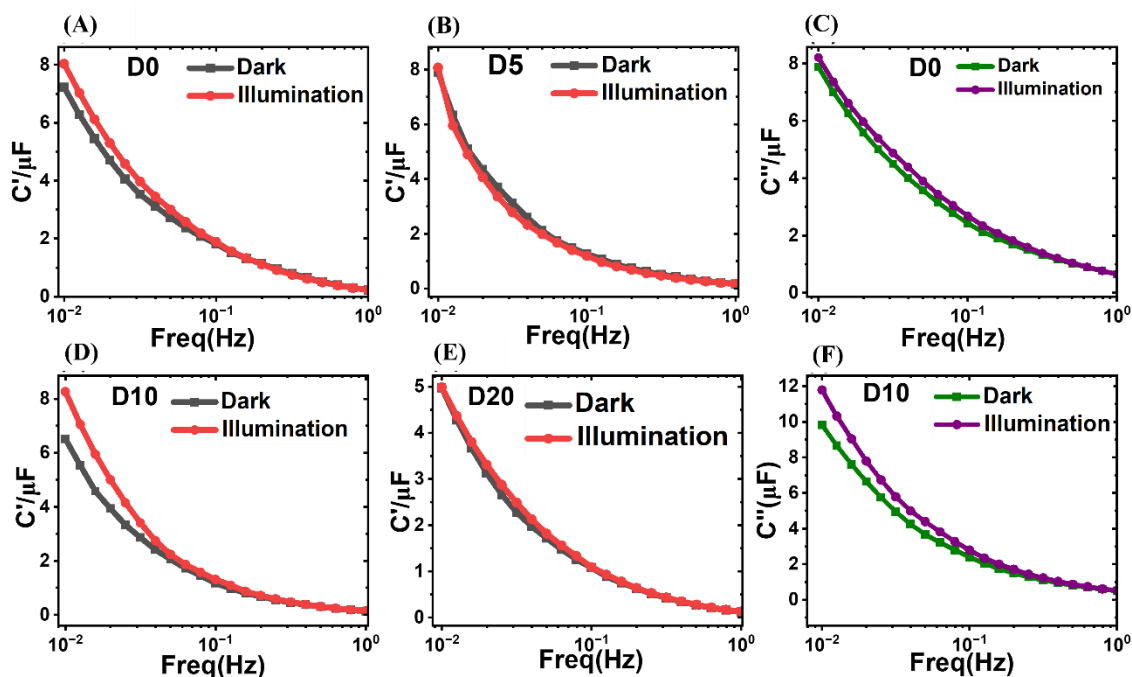
Figure S18. Real part of capacitance (C') versus frequency calculated from EIS spectra for Devices D0 (A), device D5 (B), device D10 (C), device D10 (D), under dark (black) and illuminated condition (red). The imaginary part of capacitance under dark and illumination for device D0 (E), and for device D10 (F) at various scan rates.

These all devices demonstrate that C' is very low at higher frequencies, indicating that there is no energy storage at these frequencies. The real part of the capacitance starts to rise from mid to low frequencies and rises quickly until it approaches 0.01Hz, when it achieves its maximum value. The increase in the real part of the capacitance is directly attributed to the storage of energy in the device. The variation in the real part of the capacitance for the device D10 also illustrates the higher specific capacitance under illumination. It is shown in **SI Figure S18(A)**, C' is increased from 7.2 μF (in Dark) to 8.2 μF (Under Illumination) for D0 device but it has been increased from 6.5 μF (in Dark) to 8.2 μF (Under Illumination, ~26%) for the device D10 at 0.01Hz shown in **SI Figure S18(C)**. Consequently, we can conclude that D10 has shown the greatest increment under illumination, as shown by the CV curve. By looking at the curve between imaginary capacitance (C") vs frequency it can be seen in the

curve that C" began to increase at a higher frequency under illumination than that under darkness for the device D0 and D10, as shown in **SI Figure S18(E & F)**. So, it can be concluded that device D10 start to store the charge at low frequency under illumination than in the dark.
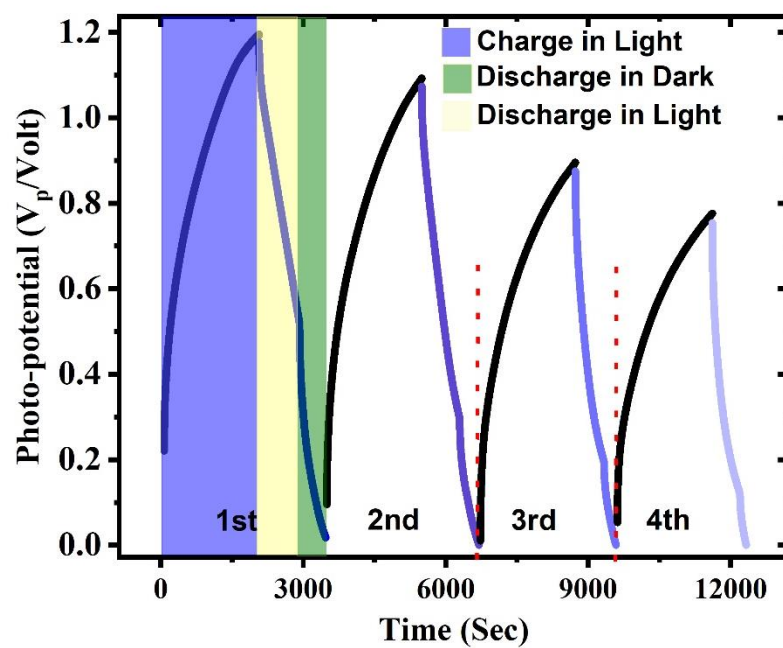
Figure S19. Stability test under illumination using GCD measurement with charging by 0 Ag^{-1} and discharging by 50 mAg^{-1}

(A)

(B)

(C)

(D)
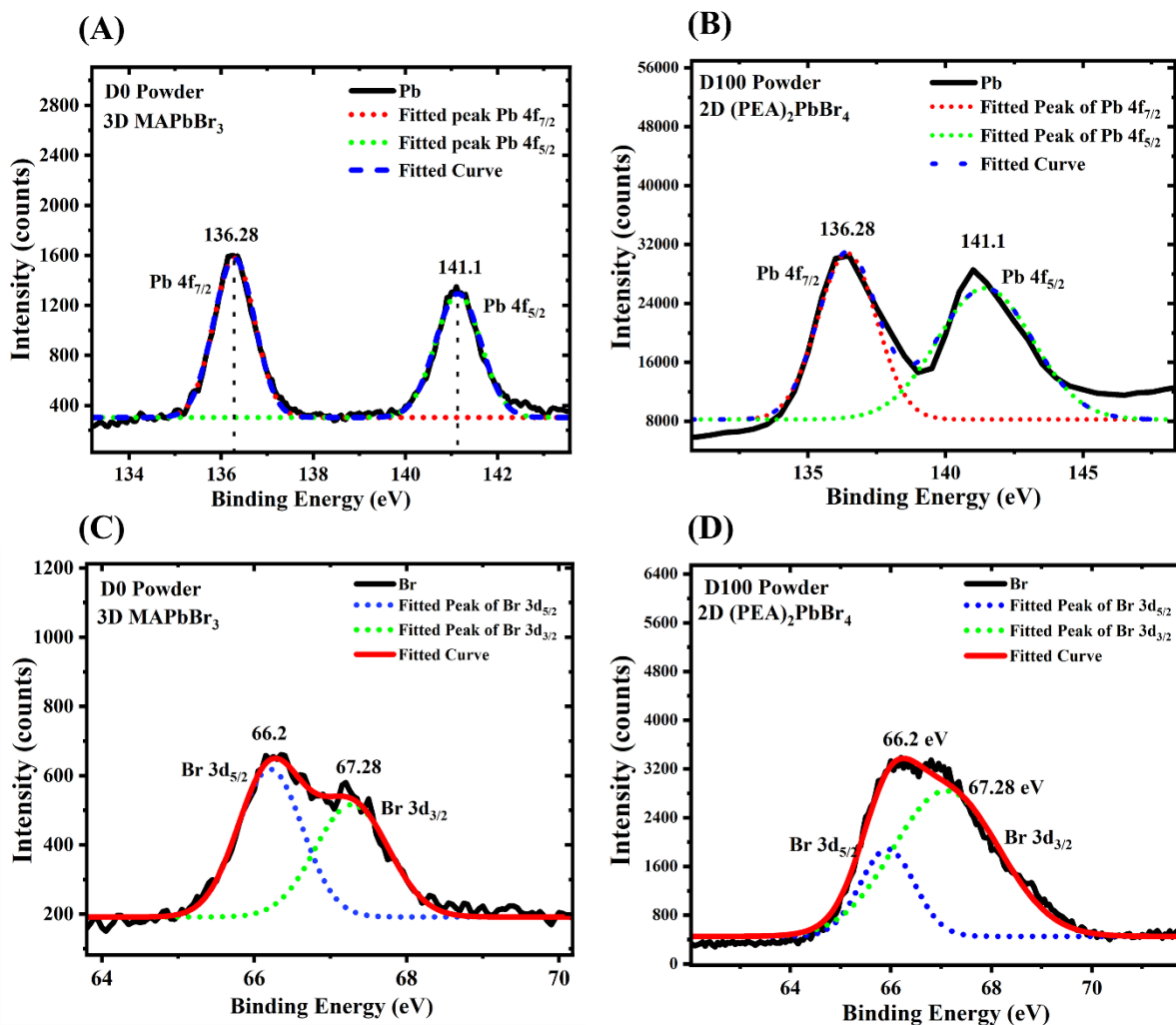
Figure S20. X-ray photoelectron spectroscopy for powder of pure 3D (MAPbBr3) and 2D ((PEA)2PbBr4) perovskite for Pb 4f (A and B) and Br 3d (C and D).

We have performed XPS measurements on 2D and 3D perovskite materials to look at potential differences in the chemical environment and valence state of the pure 3D perovskite and 2D perovskite powder. An orbital splitting difference of around 4.82 eV was seen in Pb 4f spectra, where Pb $4f_{5/2}$ and Pb $4f_{7/2}$ are aligned at 141.1 eV and 136.28 eV, respectively directly correlate to Pb^{2+} cations for 3D and 2D based perovskite powder which signifies that there is no significant change in the spectra of Pb 4f due to the change in the dimension of the perovskite material. We can conclude that the physical mixing of the 2D perovskite material in 3D

perovskite material does not change the binding energy of the Pb. Additionally, orbital splitting of Br $3d_{5/2}$ (66.2 eV) and Br $3d_{3/2}$ (67.28 eV) for MAPbBr3 have been discovered in Br 3d core-level spectra. Similarly, the Br 3d spectrum peak in 2D perovskite powder was observed in the same position without changing in the binding energies, showing that physical mixing in the 3D/2D based materials did not change the chemical environment of $[PbBr6]^{-4}$ octahedra and the Pb-Br interactions.

Calculation:

The following equation may be used to determine the photo-charge conversion efficiency (η) for the electrode containing 2% carbon when a light source with a power of 70 mW cm^{-2} at a wavelength of 405 nm is used:

$$\eta = \frac{E_{OUT}}{E_{IN}} \times 100\%$$

$$\eta = \frac{E_m \times m}{P_{IN} \times discharging\ time(t) \times Area(cm^2)} \times 100\%$$

For D0- Electrode:

Energy density $= \frac{C \times (\Delta V)^2}{7.2} = 4.699$ W h Kg^{-1}

$$\eta = \frac{4.699 \times 0.001 \times 3600}{70 \times 1149 \times 1} \times 100\%$$

$$\eta = 0.021\% = \sim 0.02\%$$

For D10 – Electrode:

Energy density $= \frac{C \times (\Delta V)^2}{7.2} = 6.33$ W h Kg^{-1}

$$\eta = \frac{6.33 \times 0.001 \times 3600}{70 \times 1196 \times 1} \times 100\%$$

$$\eta = 0.028\% = \sim 0.03\%$$

Where, E_m (=4.699 W h kg^{-1} for D0 and 6.33 W h kg^{-1} for D10) and m (=1 mg) are the energy density and active mass of the photo-ion capacitors. P_{IN} is the power/intensity (70 mW cm^{-2}) of the illuminated light. t is the discharging time in the light which is 1149 sec and 1196 sec for D0 and D10, respectively at 50 mA g^{-1} and the active surface area of the electrode was 1cm^2.

Table S3: Comparison of the photo-voltage and photo-charge conversion efficiency of our work with perilous photo rechargeable/integrated energy storages devices.

Photorechargeable energy storage device	Photovoltage response	Photo-charge conversion efficiency	Light source	Journal/Year	Ref.
LiFePo4/N719- dye//Li-batteries	3.65 V	0.06%	100 mW cm^{-2}	*Nature Commun. 2017*	1
2D Halide perovskite//Li-batteries	3.0 V	0.034%	420- 650 nm illumination	*Nano Letter 2018*	2
V$_2$O$_5$//Li-batteries	2.82 V	2.6%	455 nm illumination	*Nano Letter 2020*	3
VO$_2$/ZnO//Zn-batteries	880 mV	0.51%	455 nm illumination	*J. Mater. Chem. A, 2021*	4
VO$_2$//Zn-batteries	890 mV	0.18%	455 nm illumination	*Adv. Energy Mater. 2021*	4
MoS2/Zn-batteries	940 mV	1.8% and 0.2%	455 nm illumination and @ 1 Sun	*ACS Nano 2022*	5
AC/V$_2$O$_5$ zinc ion capacitors	500 mV	0.05%	455 nm illumination	*ACS Energy Lett. 2020*	6
ITO BR/P3HT based Photorechargeable supercapacitors	280 mV	0.0017%	100 mW cm^{-2}	*ACS Appl. Mater. Interfaces 2021*	7

3D Hybrid halide perovskite Photorechargeable supercapacitors	325 mV	~0.02%	20 mW cm^{-2} (White LED source)	*ACS Appl. Mater. Interfaces 2022*	8
TiO2//TiO2 SC and DSSC	610mV	1.64%	100 mW cm^{-2}	*Adv. Funct. Mater.*	9
CNTs-TiO2//CNTs-TiO2 SC and DSSC	600mV	1.5%	100 mW cm^{-2}	*Angew. Chem. - Int. Ed. 2012*	10
MWCNTs//MWCNTs SC and DSSC	650mV	1.83%	100 mW cm^{-2}	*Adv. Mater. 2014*	11
TiO2//MWCNTs SC and polymer solar cell	400mV	0.82%	100 mW cm^{-2}	*Adv. Mater. 2014*	12
PEDOT-carbon//PEDOT carbon SC and PSC	710mV	4.7%	100 mW cm^{-2}	*Adv. Mater. Technol. 2016*	13
CF@TiO2@MoS2//CF@ TiO2 @MoS2 SC and DSSC	750mV	1.8%	45 to 100 mW cm^{-2}	*J. Mater. Chem. A 2018*	14
V$_2$O$_5$//Zn-batteries	950 mV	1.2%	455 nm illumination	*Energy Environ. Sci. 2020*	15
g-C3N4//Zn-ion capacitors	850 mV	0.01%	420 nm illumination	*Nano Letter. 2020*	16
3D-2D dimensional based Engineering	1115 mV For D0 and 1190 mV for D10	0.021% And 0.028%	405nm illumination, 70mW cm^{-2}	*This Work*	

References:

(1)   Paolella, A.; Faure, C.; Bertoni, G.; Marras, S.; Guerfi, A.; Darwiche, A.; Hovington, P.; Commarieu, B.; Wang, Z.; Prato, M.; Colombo, M.; Monaco, S.; Zhu, W.; Feng, Z.; Vijh, A.; George, C.; Demopoulos, G. P.; Armand, M.; Zaghib, K. Light-Assisted Delithiation of Lithium Iron Phosphate Nanocrystals towards Photo-Rechargeable Lithium Ion Batteries. *Nat. Commun.* **2017**, *8*. https://doi.org/10.1038/ncomms14643.

(2)   Ahmad, S.; George, C.; Beesley, D. J.; Baumberg, J. J.; De Volder, M. Photo-Rechargeable Organo-Halide Perovskite Batteries. *Nano Lett.* **2018**, *18* (3), 1856–1862. https://doi.org/10.1021/ACS.NANOLETT.7B05153/ASSET/IMAGES/MEDIUM/NL-2017-05153Q_M002.GIF.

(3)   Boruah, B. D.; Wen, B.; De Volder, M. Light Rechargeable Lithium-Ion Batteries Using V2O5Cathodes. *Nano Lett.* **2021**, *21* (8), 3527–3532. https://doi.org/10.1021/acs.nanolett.1c00298.

(4)   Deka Boruah, B.; Mathieson, A.; Park, S. K.; Zhang, X.; Wen, B.; Tan, L.; Boies, A.; De Volder, M. Vanadium Dioxide Cathodes for High-Rate Photo-Rechargeable Zinc-Ion Batteries. *Adv. Energy Mater.* **2021**, *11* (13), 2100115. https://doi.org/10.1002/aenm.202100115.

(5)   Boruah, B. D.; Wen, B.; De Volder, M. Molybdenum Disulfide-Zinc Oxide Photocathodes for Photo-Rechargeable Zinc-Ion Batteries. *ACS Nano* **2021**, *15* (10), 16616–16624. https://doi.org/10.1021/acsnano.1c06372.

(6)   Boruah, B. D.; Wen, B.; Nagane, S.; Zhang, X.; Stranks, S. D.; Boies, A.; De Volder, M. Photo-Rechargeable Zinc-Ion Capacitors Using V2O5-Activated Carbon Electrodes. *ACS Energy Lett.* **2020**, *5* (10), 3132–3139. https://doi.org/10.1021/acsenergylett.0c01528.

(7)   Dong, W. J.; Cho, W. S.; Lee, J. L. Indium Tin Oxide Branched Nanowire and Poly(3-Hexylthiophene) Hybrid Structure for a Photorechargeable Supercapacitor. *ACS Appl. Mater. Interfaces* **2021**, *13* (19), 22676–22683. https://doi.org/10.1021/acsami.1c05241.

(8)   Kumar, R.; Kumar, A.; Shukla, P. S.; Varma, G. Das; Venkataraman, D.; Bag, M. Photorechargeable Hybrid Halide Perovskite Supercapacitors. *ACS Appl. Mater. Interfaces* **2022**, *14* (31), 35592–35599. https://doi.org/10.1021/ACSAMI.2C07440.

(9)   Xu, J.; Wu, H.; Lu, L.; Leung, S. F.; Chen, D.; Chen, X.; Fan, Z.; Shen, G.; Li, D. Integrated Photo-Supercapacitor Based on Bi-Polar TiO2 Nanotube Arrays with Selective One-Side Plasma-Assisted Hydrogenation. *Adv. Funct. Mater.* **2014**, *24* (13), 1840–1846. https://doi.org/10.1002/adfm.201303042.

(10)   Chen, T.; Qiu, L.; Yang, Z.; Cai, Z.; Ren, J.; Li, H.; Lin, H.; Sun, X.; Peng, H. An Integrated "Energy Wire" for Both Photoelectric Conversion and Energy Storage. *Angew. Chemie - Int. Ed.* **2012**, *51* (48), 11977–11980. https://doi.org/10.1002/anie.201207023.

(11)   Yang, Z.; Deng, J.; Sun, H.; Ren, J.; Pan, S.; Peng, H. Self-Powered Energy Fiber: Energy Conversion in the Sheath and Storage in the Core. *Adv. Mater.* **2014**, *26* (41), 7038–7042. https://doi.org/10.1002/adma.201401972.

(12)   Zhang, Z.; Chen, X.; Chen, P.; Guan, G.; Qiu, L.; Lin, H.; Yang, Z.; Bai, W.; Luo, Y.; Peng, H. Integrated Polymer Solar Cell and Electrochemical Supercapacitor in a Flexible and Stable Fiber Format. *Adv. Mater.* **2014**, *26* (3), 466–470. https://doi.org/10.1002/adma.201302951.

(13)   Xu, J.; Ku, Z.; Zhang, Y.; Chao, D.; Fan, H. J. Integrated Photo-Supercapacitor Based on PEDOT Modified Printable Perovskite Solar Cell. *Adv. Mater. Technol.* **2016**, *1* (5), 1–5. https://doi.org/10.1002/admt.201600074.

(14)   Liang, J.; Zhu, G.; Lu, Z.; Zhao, P.; Wang, C.; Ma, Y.; Xu, Z.; Wang, Y.; Hu, Y.; Ma, L.;

Chen, T.; Tie, Z.; Liu, J.; Jin, Z. Integrated Perovskite Solar Capacitors with High Energy Conversion Efficiency and Fast Photo-Charging Rate. *J. Mater. Chem. A* **2018**, *6* (5), 2047–2052. https://doi.org/10.1039/c7ta09099d.

(15)   Boruah, B. D.; Mathieson, A.; Wen, B.; Feldmann, S.; Dose, W. M.; De Volder, M. Photo-Rechargeable Zinc-Ion Batteries. *Energy Environ. Sci.* **2020**, *13* (8), 2414–2421. https://doi.org/10.1039/d0ee01392g.

(16)   Boruah, B. D.; Mathieson, A.; Wen, B.; Jo, C.; Deschler, F.; De Volder, M. Photo-Rechargeable Zinc-Ion Capacitor Using 2D Graphitic Carbon Nitride. *Nano Lett.* **2020**, *20* (8), 5967–5974. https://doi.org/10.1021/acs.nanolett.0c01958.